Li *et al. Heritage Science* (2022) 10:84
https://doi.org/10.1186/s40494-022-00720-7

Heritage Science

RESEARCH Open Access

Apatite in *Hamipterus tianshanensis* eggshell: advances in understanding the structure of pterosaur eggs by Raman spectroscopy

Ying Li[1,2], Xufeng Zhu[2,3,4], Qiang Wang[2,4], Shunxing Jiang[2,4], Yimin Yang[1,2], Wugan Luo[1,2*] and Xiaolin Wang[2,3,4*]

Abstract

Pterosaur eggs can offer information about pterosaur reproductive strategies and are extremely precious because only a small number of specimens have been discovered. Previous studies have mainly focused on morphological descriptions of pterosaur eggs and their embryos while the chemical composition of pterosaur eggs has received little attention. The conventional view believed that the eggshell was composed of calcite. However, previous SEM–EDS results for *Hamipterus tianshanensis* showed that the eggshell contains phosphorus. Therefore, the object of this research is to determine the mineral composition of the eggshell of *H. tianshanensis*. Two eggs were analyzed by scanning electron microscopy coupled with energy dispersive X-ray spectrometry (SEM–EDS) and Raman spectroscopy. The SEM–EDS results show that both surface and cross section are porous and characterized by small irregularly shaped particulates. Moreover, the distribution of Ca and P has a strict coincidence in the cross-section of eggshells. Furthermore, neither the intense peaks of calcite nor organic peaks can be observed by Raman spectroscopy in eggshells. Meanwhile, the Raman spectroscopy mapping analysis result shows a sharp and intense peak at approximately 966 cm^{-1} among the white eggshell, which can be hard evidence that *H. tianshanensis* eggs are mainly composed of calcium phosphate. Combined with the present of F in the eggshell, it can be inferred that fluorapatite $Ca_5(PO_4)_3F$ is the main mineral. The fluorapatite eggshell can be interpreted in two ways. One explanation is that *H. tianshanensis* laid apatite-shelled eggs, similar to living *Salvator merianae*, and the bioapatite transformed to fluorapatite over geological time. Another possible explanation is that the fluorapatite comes from the result of phosphatization of soft egg membrane tissues through taphonomic processes, indicating that *H. tianshanensis* might have laid soft eggs. Regardless, the results show that fluorapatite, rather than calcite is the main preserved mineral composition of *H. tianshanensis* eggshell, correcting the previous view. This study contributes to the present understanding of the mineral composition of pterosaur eggshells and may offer some insight into the pterosaur reproduction pattern.

Keywords: Early Cretaceous, Pterosaur eggs, Soft eggshell, SEM–EDS, Biomineralization, Phosphatization

Introduction

Raman spectroscopy, because of its ability to perform non-destructive in-situ analysis, with little or no sample preparation, is an ideal method to analyze precious relics and is widely used in analyzing their composition. For example, analysis of corrosion products on bronze artifacts [1]; analysis of the pigments and dyestuff [2–6], especially for the cobalt blue pigment [7], Chinese Blue ($BaCuSi_4O_{10}$), and Chinese Purple ($BaCuSi_2O_6$) [7]; identification of the firing temperature of ancient ceramics

*Correspondence: xiahua@ucas.ac.cn; wangxiaolin@ivpp.ac.cn

[1] Department of Archaeology and Anthropology, University of Chinese Academy of Sciences, Beijing 100049, China
[2] Key Laboratory of Vertebrate Evolution and Human Origins of Chinese Academy of Sciences, Institute of Vertebrate Paleontology and Paleoanthropology, Chinese Academy of Sciences, Beijing 100044, China
Full list of author information is available at the end of the article

[8]; and identification of Chinese jades [9] and glass beads [10].

In addition to cultural heritage, Raman spectroscopy also plays an important role in paleontology studies. Firstly, it is a powerful tool to identify fossil damage, especially sulfate efflorescence [11]. Secondly, it is useful for detecting the chemical composition of fossils, such as identifying minerals in wood fossils [12], root fossils (rhizoliths) [13], insect cuticle fossils [14], microscopic fossils [15], and ctenophore embryos [16]. Moreover, Raman spectroscopy is powerful for detecting organic matter, such as organics in the silica matrix [17] and kerogen in fossils [14, 18]. Moreover, N-heterocyclic polymers in fossils can provide clues about how proteinaceous tissues undergo diagenesis [19]. Thirdly, Raman spectroscopy spectra can be used to determine the diagenetic degree, which is important for other analyses carried out on fossils, such as isotope analysis [20, 21].

Fossil eggs, as valuable specimens, can provide reproductive information on amniotes [22] and paleoenvironmental and taphonomy information [23, 24]. Meanwhile, Raman spectroscopy, as a non-destructive test, has drawn much attention in fossil egg researchers. For example, Raman spectroscopy can be used to identify the chemical composition of fossil eggshell [25], such as the hydroxyapatite (HAP) preserved in the cuticle layer [26], phosphate in the membrane [27], and color-producing pigments [28–30], S- to N-heterocycles [31], and amorphous carbon [32]. Moreover, Raman spectroscopy with the deconvolution technique can be used to detect the maximum paleotemperature recorded in eggshells [33].

Most researchers focus on hard-shelled eggs (such as dinosaur eggs), while there are few studies on softshell specimens. Mainly because the soft eggs have poor preservation potential, and only a small number of cases have been reported [34–36]. To obtain more information from these valuable and rare soft egg specimens, researchers have shown an increased interest in element and chemical analysis [37], especially in using Raman spectroscopy for its non-destruction. Recently, Raman spectroscopy has played an important role in soft egg studies, such as a giant egg from the Late Cretaceous of Antarctica (*Antarcticoolithus*) [35], the ornithischian *Protocertops*, and the basal sauropodomorph *Mussaurus* eggs [36].

The eggs of *Hamipterus tianshanensis*, with calcareous hard eggshell followed by a soft membrane [38], have gained much influence since they were first reported. Similar to the comments by David M. Martill [39], never before have so many pterosaur eggs been found in such concentrated conditions. Taking the most important section in the sandstone block (3.28 m^2) as an example (Fig. 1c), more than 200 eggs have been yielded, while more are uncountable and buried under the exposed eggs [40]. This discovery provides a unique opportunity to investigate pterosaur reproduction and early growth [40]. However, little research has focused on the eggs of *H. tianshanensis,* and more information is still needed, for example, the mineral composition of the white shell of *Hamipterus* eggs.

A previous study believed that the eggshell was composed of calcite, similar to most reptiles [38]. However, the SEM–EDS results presented in that work showed that the shell contained phosphorus [38]. Therefore, it is unclear which kind of phosphorus-rich minerals exists in the *Hamipterus* eggshell. Moreover, how are calcite- and phosphorus-rich minerals distributed over the eggshell? The specific objective of this study is to answer these questions. The findings should make an important contribution to the field of pterosaur eggs. In addition, there are few studies on pterosaur eggs because only a few specimens have been reported [41–49], so this study can supply more information about pterosaur egg structure.

In this study, with the support of SEM–EDS pre-observation, micro-Raman spectroscopy analysis coupled with an optical microscope was carried out to identify the white eggshell composition and the mineral distribution of *Hamipterus* pterosaur eggs. This study can provide important information about the characteristics of pterosaur eggs and the taphonomy of *Hamipterus* pterosaur.

Materials and methods

Materials

Bones and eggs of *H. tianshanensis* were collected from 2006 to 2016 at the Turpan-Hami Basin, Xinjiang Uygur Autonomous Region, northwestern China (Fig. 1a). According to the geological studies done in this region, the layers where the fossils were found were fall into part of the Lower Cretaceous Tugulu Group [40, 50]. The fossil bearing strata is consisted of gray sandstones with coarse cross bedding and grayish-white fine sandstones with parallel beddings and coarser reddish-brown sandstones (Fig. 1b) [40]. Almost *Hamipterus* specimens and their eggs were found in tempestite interlayers.

The two specimens involved in this research were all eggs of *H. tianshanensis* from Hami. Both specimens were collected in layer f (Fig. 1b) and now they are preserved in the Institute of Vertebrate Paleontology and Paleoanthropology, Chinese Academy of Sciences.

Sample no. 1 (IVPP V 18939) was cut for SEM–EDS analysis several years ago [38]. This specimen was analyzed by a non-destructive method because it is from the museum's collection storeroom and should be returned. The eggshell of sample no. 1 is in good condition (Fig. 2f, h), and only a few areas are exfoliated (Fig. 2g). Sample no. 2 is a half fossil egg and can be analyzed by destructive methods if necessary. The eggshell of sample no. 2 is

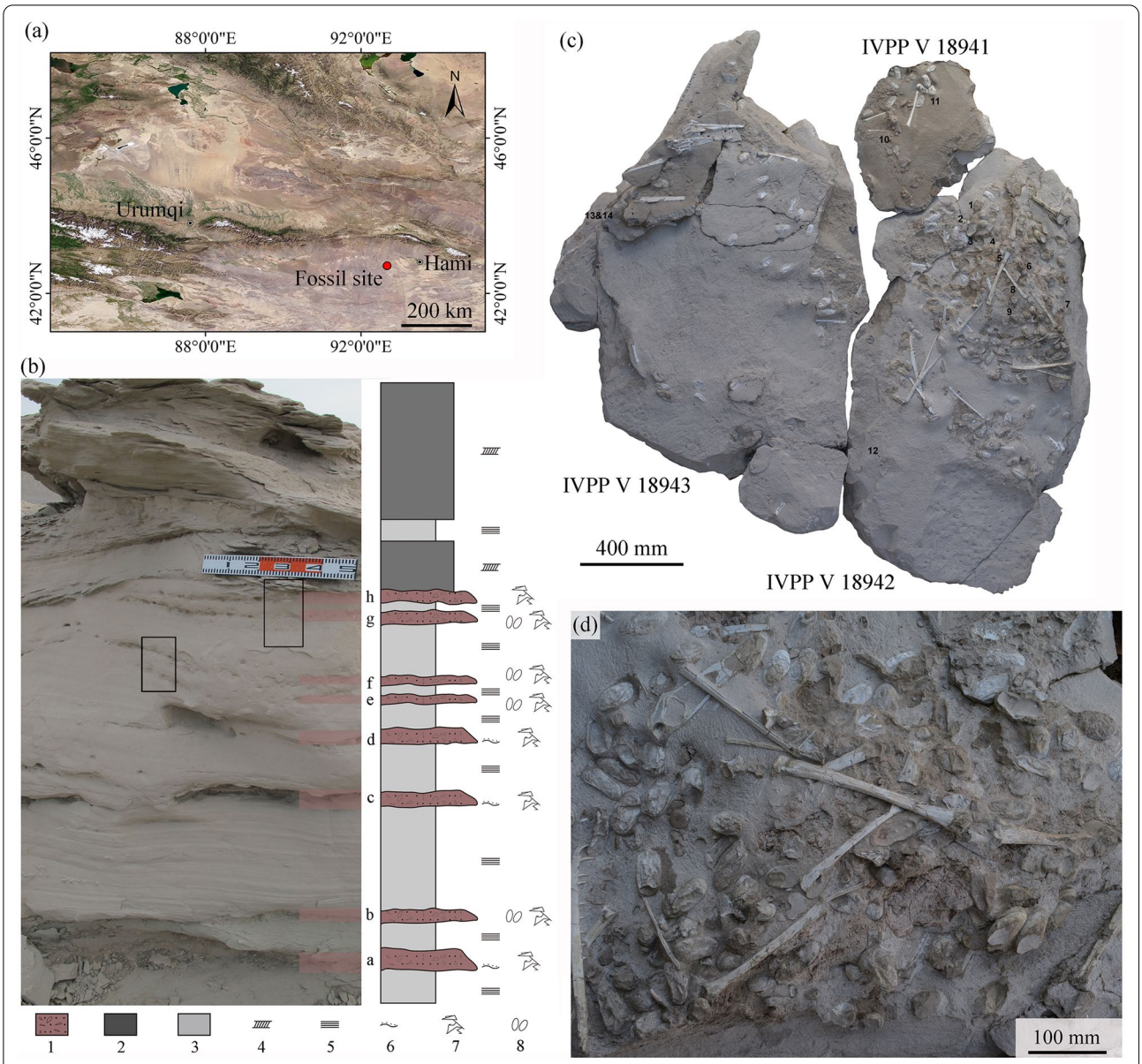

Fig. 1 **a** Map showing the fossil site. **b** Section of the fossil bearing strata, and layer f is the main level where specimens of **c** were collected. Two specimens in this article were also collected in layer f (legend: 1, coarse grained sandstone with pellets; 2, middle grained sandstone; 3, fine sandstone; 4, cross beddings; 5, parallel beddings; 6, scour marks; 7, pterosaur bones; 8, pterosaur eggs). **c** Eggs of *H. tianshanensis* preserved with pterosaur bones in sandstone (IVPP V 18941–18943). **d** The close-up view of egg fossils (IVPP V 18942). Figure 1b, c, d reproduced with permission of Ref. [40], Copyright of ©2017 Science

in poor condition because many eggshell areas have exfoliated during removing the matrix (Fig. 3d). Only a small area is relatively well preserved (Fig. 3c). Furthermore, a small area is covered with matrix on both sides and therefore can be regarded as well preserved with no exfoliation (Fig. 3e). Both specimens are preserved in three dimensions and contain no embryos.

Methods

SEM–EDS

Phenom XL with a 100 mm * 100 mm sample size was used to observe sample no. 1b because sample no. 1a is too large to analyze. A small part of the egg was cut off from specimen no. 2. The sample was gold-coated and imaged by Phenom Pro X. Both Phenom desktop scanning electron microscopes (SEM) were equipped with

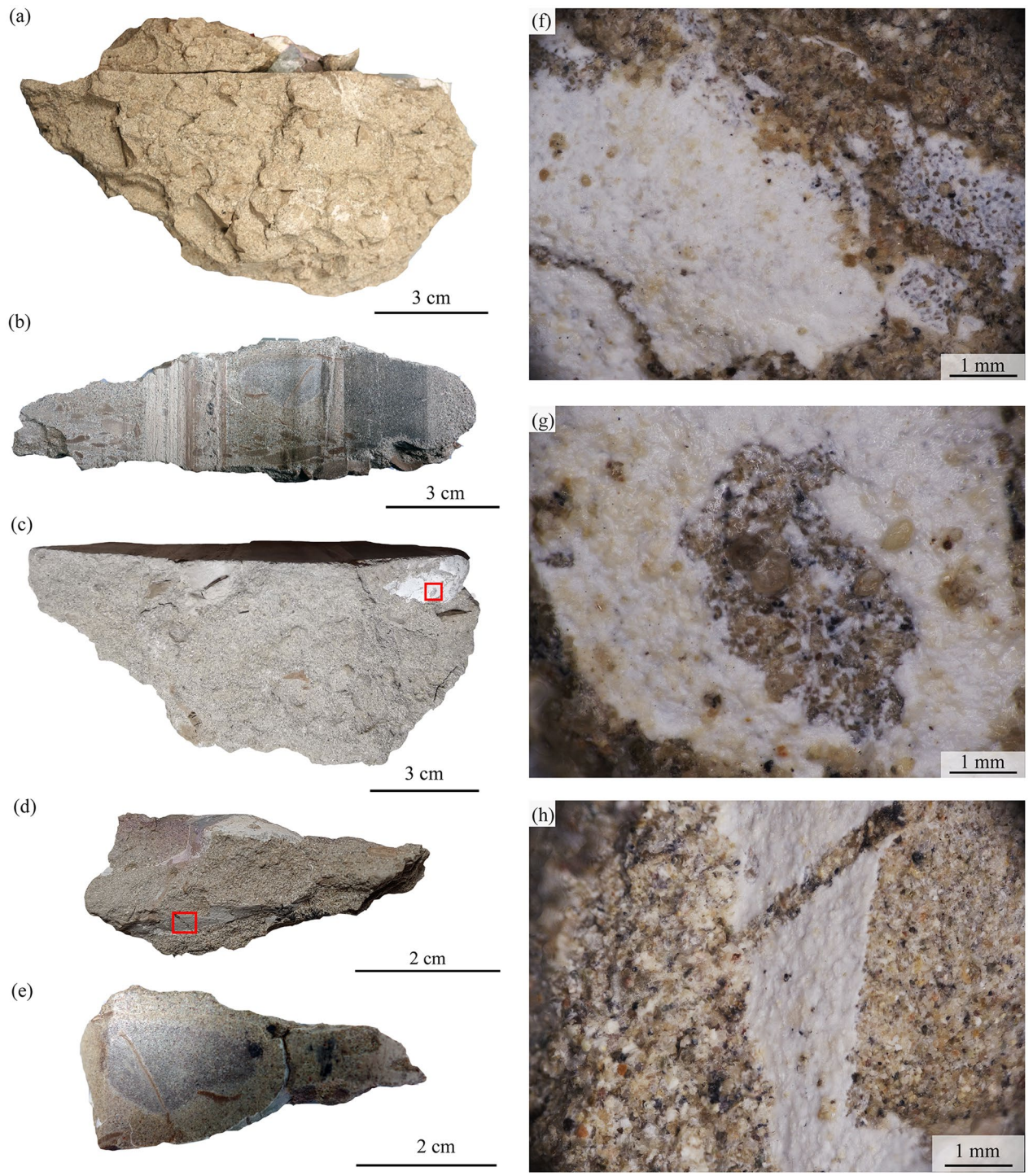

Fig. 2 *Hamipterus tianshanensis* egg Sample no. 1 (IVPP V 18939). This sample was cut for SEM–EDS analysis in Wang et al. [38]. **a** Eggs pieces together (front view). **b, c** The bigger cut part, numbered Sample no. 1a. **d, e** The smaller counterpart, numbered Sample no. 1b. **f** The microstructure of eggshell preserved well. **g** An enlargement of the red box in **c** shows the exfoliated area. **h** Enlargement of the red box in **d** shows the preserved well area

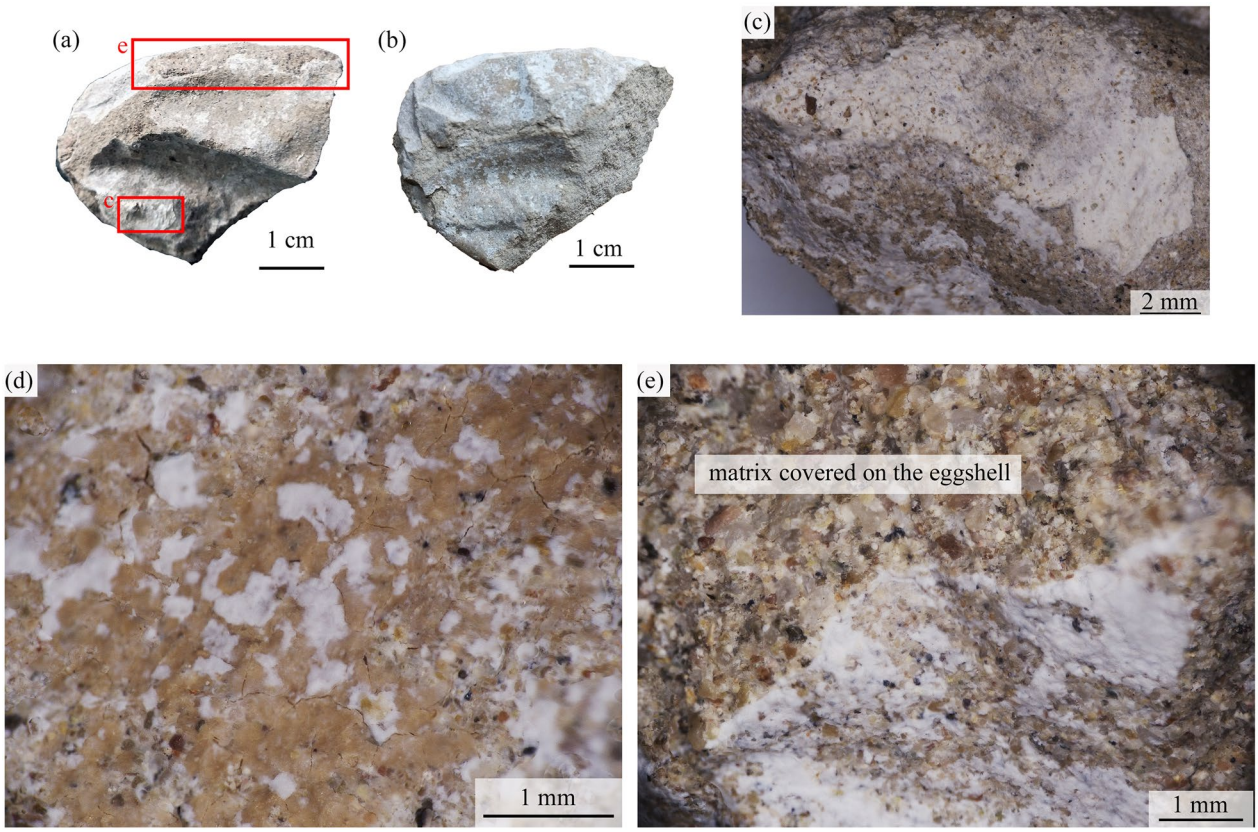

Fig. 3 *Hamipterus tianshanensis* egg Sample no. 2. **a** A half pterosaur egg. **b** Another side of this half pterosaur egg. **c** Enlargement of the only preserved well area in this sample. **d** Most areas are in poor condition, with white eggshell exfoliation. **e** The eggshell area was covered by matrix, and these areas can be recognized as non-exfoliation

a backscattered electron (BSE) detector and EDS. The operating voltage was 15kv.

Raman Both spot and mapping Raman analyses were performed by a Horiba XploRA PLUS Raman spectrometer with a 600 grooves/mm grating and a CCD detector. The Raman maps were constructed using Nikon E Plan 50 × LWD objectives, depending on the scan size.

For the spot analysis, data were collected using a laser wavelength of 532 nm (or 638 nm) and a laser power of 15 mW. The spectra were obtained in the range of 100 and 4000 cm^{-1} at an exposure time of 5 s and two data accumulations.

For the Raman spectroscopy mapping analysis, the incident beam was ~2 μm in diameter and 33 μm in penetration depth with ~15 mW power at a 532 nm laser. Spectra in the range of Raman shifts between 100 and 1500 cm^{-1} were collected from 23 × 107 spots on the eggshell cross-section with a 1 μm step. Acquisition time was 0.5 s for one spot. Integrated signals with peak fit amplitude results at 963 cm^{-1} were used for RS images.

Results

SEM–EDS

The BSD images show that the eggshell cross section is porous and charactered by irregularly shaped particulates. Some small irregularly round holes can be observed (Fig. 4a, b). The distribution patterns of Ca and P are the same, and the concentrations of Ca and P were very high in the eggshell (Fig. 4d). Meanwhile, the signal for carbon is relatively weaker in the eggshell area. The strong Ca-P signal and weak C signal indicate that eggshell may not be composed only of calcium, and some phosphorous compound must be in it. Moreover, the signals for C and N are much stronger in the outer surface area. This phenomenon can be explained by this specimen having been consolidated by some organic material after excavation. The distribution of Cl and Na has a strict coincidence (Fig. 4d). Based on the fossil bones and matrix have high content of halite [51, 52], it can be inferred that halite may also exist in the eggshell. Furthermore, the distribution patterns of Si, Al, Mg, and O are the same, indicating that the interior of eggshell is composed of quartz and feldspar.

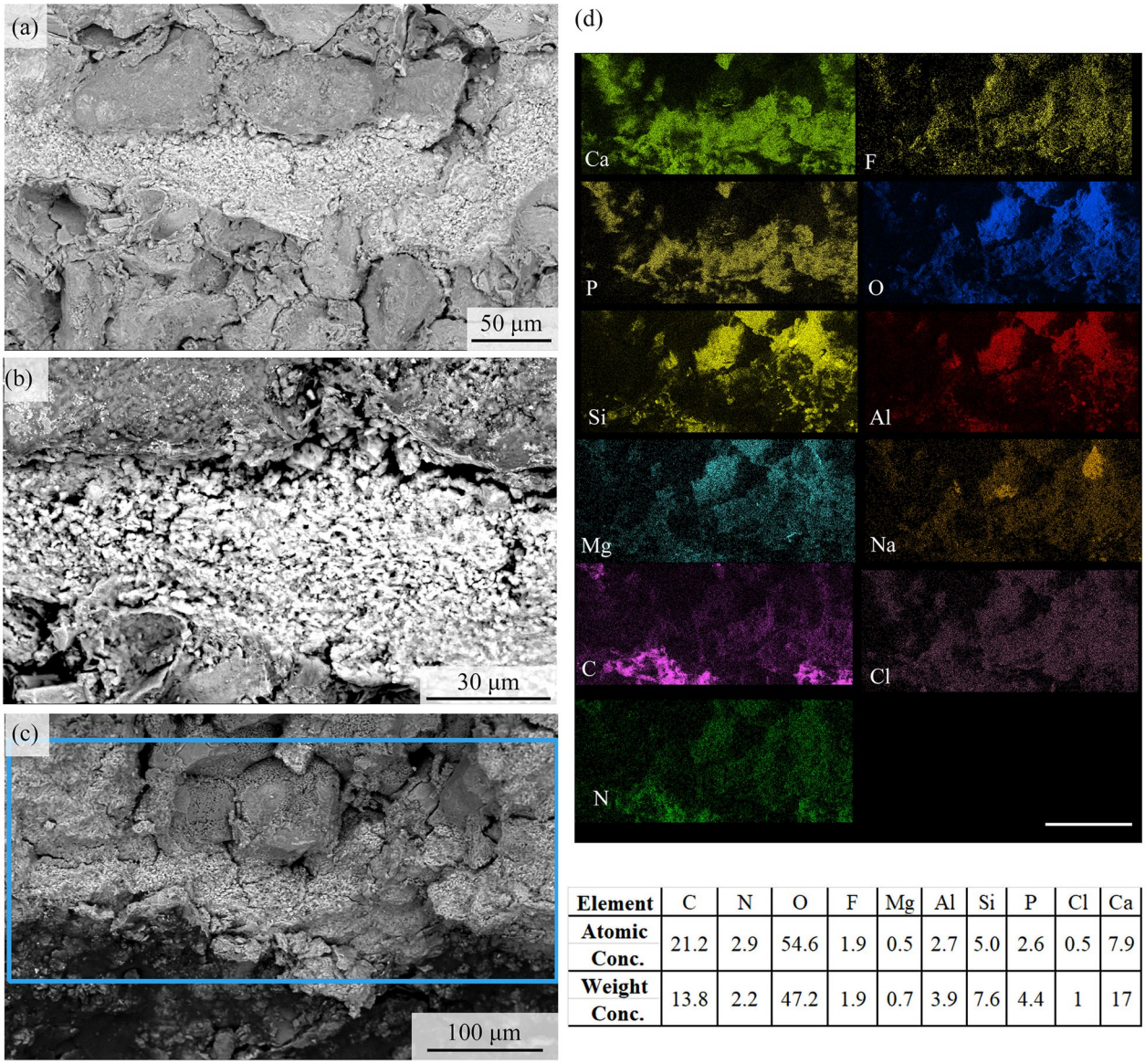

Element	C	N	O	F	Mg	Al	Si	P	Cl	Ca
Atomic Conc.	21.2	2.9	54.6	1.9	0.5	2.7	5.0	2.6	0.5	7.9
Weight Conc.	13.8	2.2	47.2	1.9	0.7	3.9	7.6	4.4	1	17

Fig. 4 SEM–EDS results for no. 1 eggshell sample (cross-section). **a** Backscatter electronic image at low magnification, outside of eggshell is up. **b** Backscatter electronic image at high magnification, outside of eggshell is up. **c** Backscatter electronic image, outside of eggshell is down. **d** Elemental mapping images of the same area for **c** (scale bar 150 μm). Outside of eggshell is down

Figures 5 and 6 show the SEM images of pterosaur egg sample no. 2 and the distribution of the elements. Both surface and cross section are characterized by small irregularly shaped particulates. Moreover, the eggshell is porous and many circular holes can be observed.

The SEM–EDS point analysis show high O, Ca, F and P peaks with minor quantities of C and Si in the eggshell (Figs. 5e and 6e). The mapping results show that the eggshell is composed of abundant concentrations of phosphorus and calcium, and Ca and P exhibit a similar distribution pattern (Fig. 6i).

The results show the same element distribution patterns in both specimens, especially for the significant phenomenon that calcium distribution is space-related to phosphorus in eggshells. The high Ca, P, and F content (> 5%) and low C content (2%) in the eggshell (Fig. 5) indicate that some phosphorus-rich minerals must be in the eggshell.

Raman spectroscopy

Raman spectroscopy was used to identify the mineral phase of pterosaur eggshell. The spot test results are

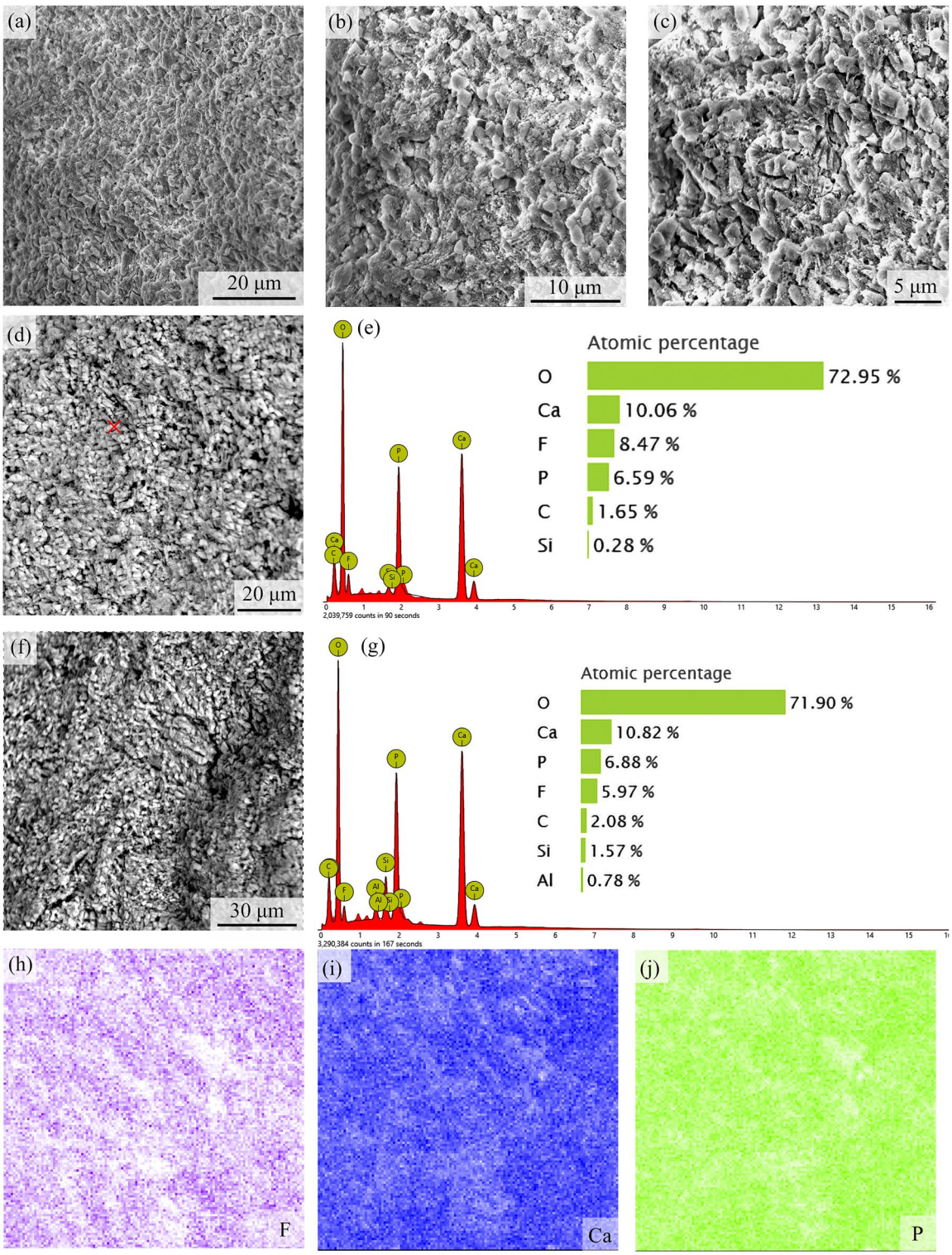

Fig. 5 SEM–EDS results for no. 2 eggshell sample (outside surface). **a, b, c** The secondary electron images of surface eggshell, small irregularly shaped particulates can be observed. **d** The backscatter electronic image of surface eggshell. **e** The elements content results in point analysis for Fig. 5d. **f** The backscatter electronic image of surface eggshell. **g** The elements content results in mapping analysis for **f**. **h** The fluorine distribution of **f**. **i** The calcium distribution of **f**. **j** The phosphorus distribution of **f**

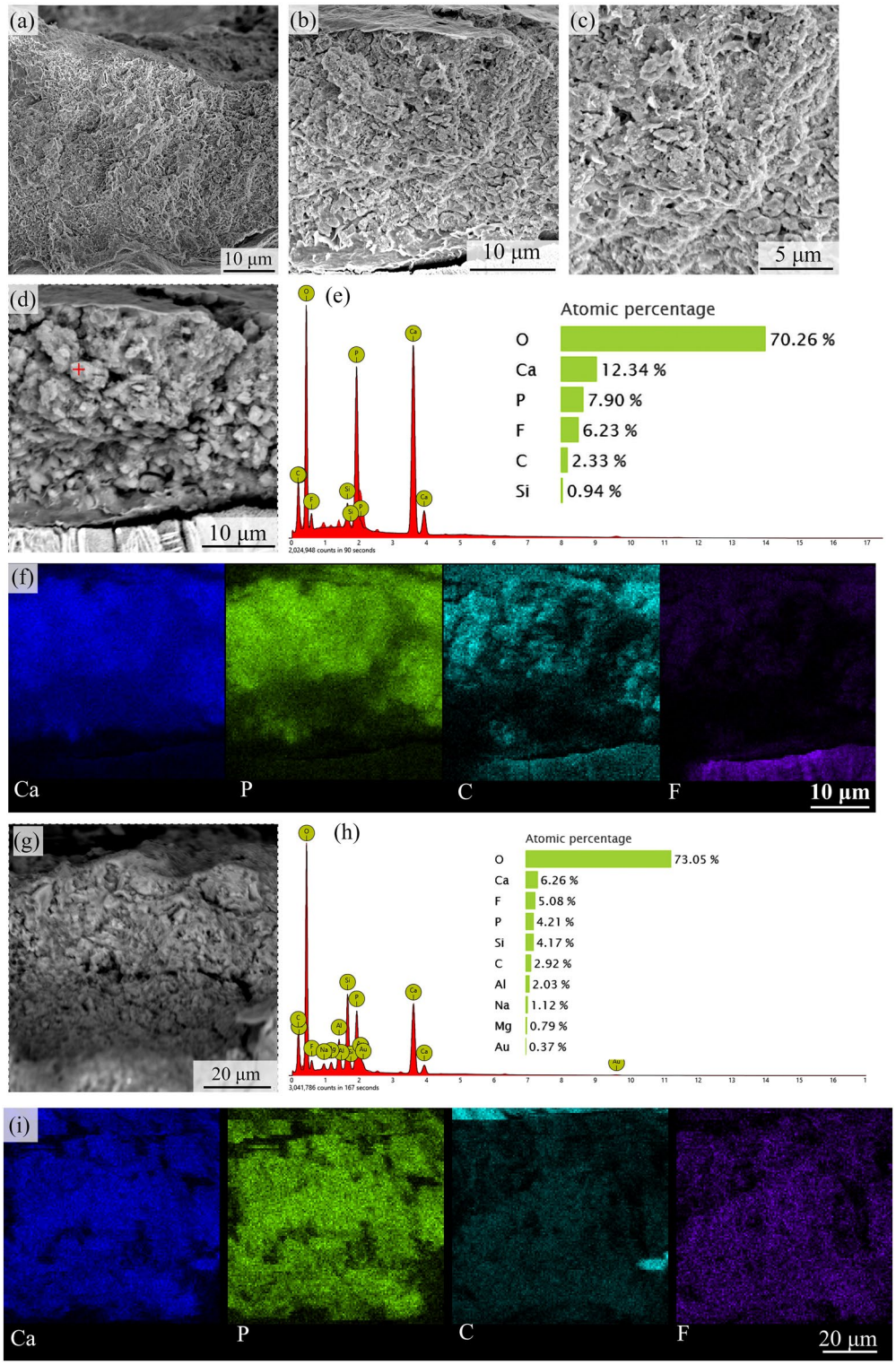

Fig. 6 SEM–EDS results for no. 2 eggshell sample (cross section). **a, b, c** The secondary electron images, small irregularly shaped particulates can be observed. **d** The backscatter electronic image. **e** The elements content results in point analysis for **d** (marked on red cross). **f** The mapping analysis results for **d**. The region at bottom of the sample (high F content) is matrix, not eggshell. **g** The backscatter electronic image. **h** The elements content results in mapping analysis for **g**. **i** The mapping analysis results for **g**. Outside of eggshell is up

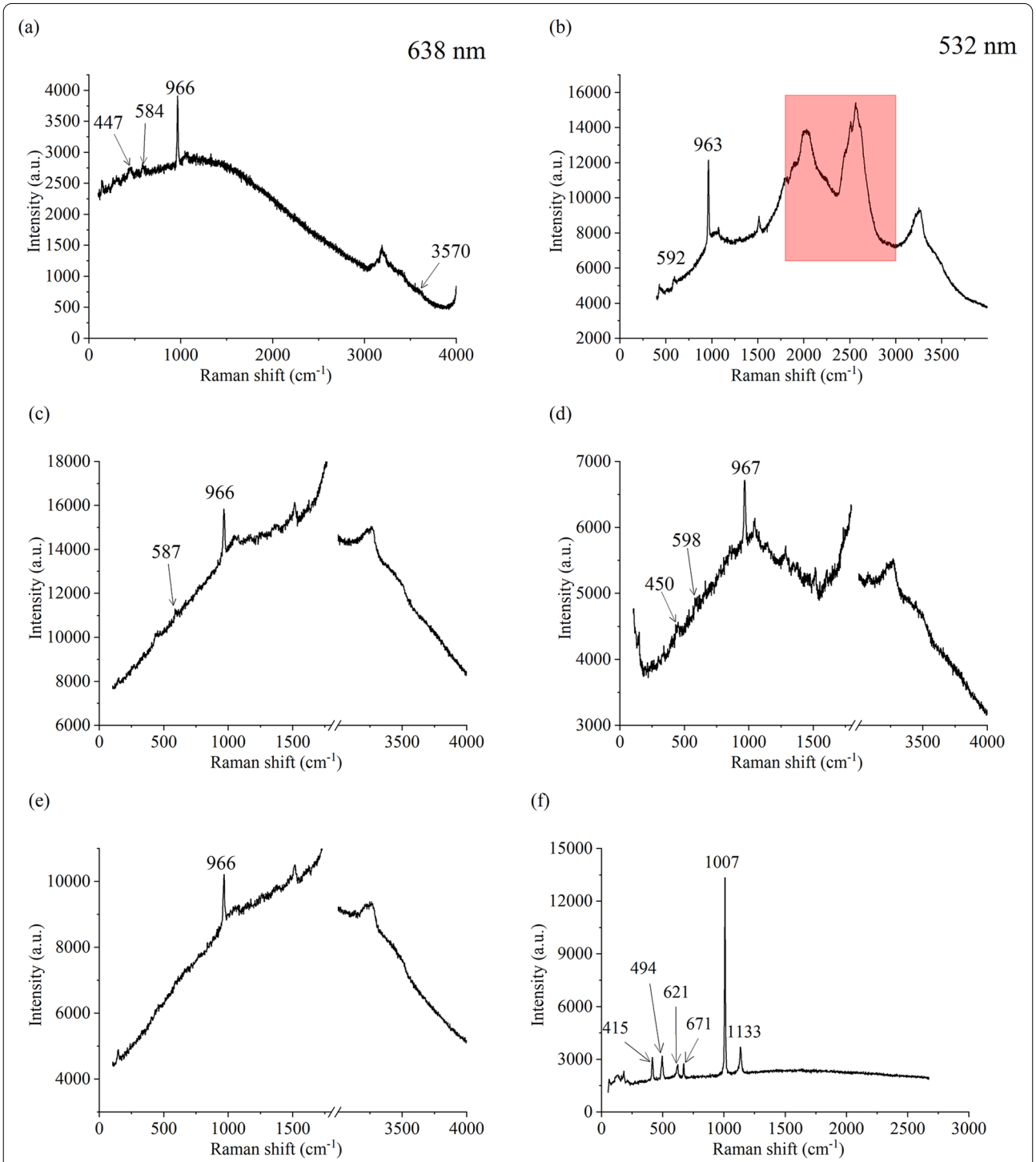

Fig. 7 Raman spectra point analysis results of samples. **a** The eggshell surface of Sample no. 2 in 638 nm. **b** The surface eggshell of Sample no. 2 in 532 nm. **c** The cross-section of Sample no. 1 in 532 nm. **d** The surface eggshell of Sample no. 1 in 532 nm. **e** The surface weathered white area of Sample no. 2 in 532 nm. **f** The surface well-preserved area (shown in Fig. 3c) of Sample no. 2 in 532 nm

presented in Fig. 7 and compared with RRUFF Raman spectroscopy databases (RRUFF Project).

Figure 7a and b are the same analysis region at different laser. It can be assured that the high broad peaks in the range of 1800–3000 cm^{-1} (marked in red box in Fig. 7b)

are the fluorescence signal. Figure 7c, d was draw in the range between 0 and 4000 cm^{-1} with a break region from 1800 to 3000 cm^{-1}.

Except for Fig. 7f, the remaining Raman spectra of the samples have the same pattern, indicating that the phosphorous compound in the eggshell is calcium phosphate. The strong band in the range 963–967 cm^{-1} corresponds to v1 stretching of the P-O band in PO_4^{3-}; the band in the range 422–454 cm^{-1} is attributed to v2 bending of the O–P–O in PO_4^{3-}; and 568–617 cm^{-1} is attributed to v4 bending PO_4^{3-} [53]. Except the white well-preserved area of sample no. 2 (Fig. 7f), all white regions of eggshell showed an intense and sharp Raman band in the range 963–967 cm^{-1}, indicating calcium phosphate in the eggshell. It is hard to recognize a band around 3570 cm^{-1} (the OH band) [54]. Combined with the existence of F element in the eggshell, it can be inferred that the white eggshell is mainly composed of fluorapatite. Moreover, the blue shift of the v 1 peak (intense peak at 966 cm^{-1} for fluorapatite while intense peak at 962 cm^{-1} for hydroxyapatite) is also the evidence of fluorapatite in the eggshell [53, 55].

Interestingly, the spectra of both samples show none of the bands at 1085 cm^{-1}, 710 cm^{-1}, 280 cm^{-1}, and 152 cm^{-1}, which are characteristic of the calcite vibrational pattern. In particular, no bands were observed at approximately 1085 cm^{-1}, which is the most characteristic and strongest band of calcite.

Figure 7f shows the Raman spectra for the well-preserved area of sample no. 2. As shown in Fig. 3c, the well-preserved white area had almost no eggshell falling off the matrix. The Raman spectroscopy results indicated that this area is composed of gypsum. The signals at 415 cm^{-1}, 494 cm^{-1}, 621 cm^{-1}, 670 cm^{-1}, 1007 cm^{-1}, and 1133 cm^{-1} are attributed to gypsum. Specifically, the strongest peak is at 1007 cm^{-1}, which is the υ1 symmetric stretch vibration mode of SO_4 tetrahedra [56]; in addition, the peaks at 415 cm^{-1} and 494 cm^{-1} are doublets for υ2 symmetric bending of SO_4 tetrahedra [57]. The peak at 1133 cm^{-1} is attributed to υ3 antisymmetric stretch vibration modes, and the peaks at 621 cm^{-1} and 670 cm^{-1} are attributed to υ4 antisymmetric bending vibration modes [56].

The gypsum on the egg surface can be attributed to making plaster-jacketed blocks during fossil collection and transportation. The large fossils were encased in plaster bandages and then moved to the laboratory for mechanical development. While making plaster-jacketed blocks, although wet tissue paper acts as a separator between the fossil and the plaster, some plaster may be covered on the exposed bones, eggs, and adjacent matrix. Thus, the white well-preserved area is not the eggshell, and it can be the residue when making plaster-jacketed blocks.

Based on the results of the Raman spot analysis, the presence of fluorapatite in the eggshell was ensured. Together with the mapping results of SEM–EDS, Ca and P have strong signals among the eggshell and exhibit a similar distribution pattern. However, carbon has a weak signal and exhibits a relatively uniform monotonous distribution between eggshell and matrix. Moreover, there is no characteristic peak of calcite. Is the pterosaur eggshell mainly composed of fluorapatite? Since single spectra obtained by spot analyses cannot give a conclusive result [58], Raman mapping was used to reveal the spatial distribution of fluorapatite.

The Raman mapping images of eggshells (sample no. 1) are shown in Fig. 8. The red areas indicate the strong signal of fluorapatite, and fluorapatite makes up the main white eggshell (Fig. 8c). However, the blue and green areas indicate that this area has a weak or no fluorapatite signal (Fig. 8c), and this area is consistent with the darker area in the optical photomicrograph, which can be related to the matrix surrounding the eggshell and the inclusion or impurity in the white eggshell (the arrow in Fig. 8b).

Based on the intense peak around 966 cm^{-1} in Raman spectrogram and the F existence in the SEM–EDS point analysis, it can be inferred that fluorapatite [$Ca_5(PO_4)_3F$] is the main mineral that composed the eggshell.

Discussion

The objective of this study is to identify what kinds of phosphorus-rich minerals existed in *Hamipterus* eggshell. The results show that the white eggshell is mainly composed of fluorapatite. Moreover, contrary to expectations, this study did not find calcite signals in eggshells. This phenomenon can be interpreted in two ways.

One possible explanation for this might be that *H. tianshanensis* laid apatite-shelled eggs, and the bioapatite transformed to fluorapatite over geological time. Although calcium carbonate is the most common chemical composition of amniotic eggs [59, 60], some reptile eggs can be composed of apatite ocassionally [61, 62]. For example, hydroxyapatite is the only biomineral present in the eggshell of *Salvator merianae,* the largest living lizard in South America [61]. It is possible that *Hamipterus* laid apatite eggs, similar to *S. merianae*. Bioapatite (biogenic hydroxyapatite) is generally unstable in a range of varying geochemical conditions and can be transformed to a more stable phase like fluorapatite. It is very common that the primary biological material (bioapatite such as bone and dental enamel) is replaced by a secondary fluorapatite phase [63, 64].

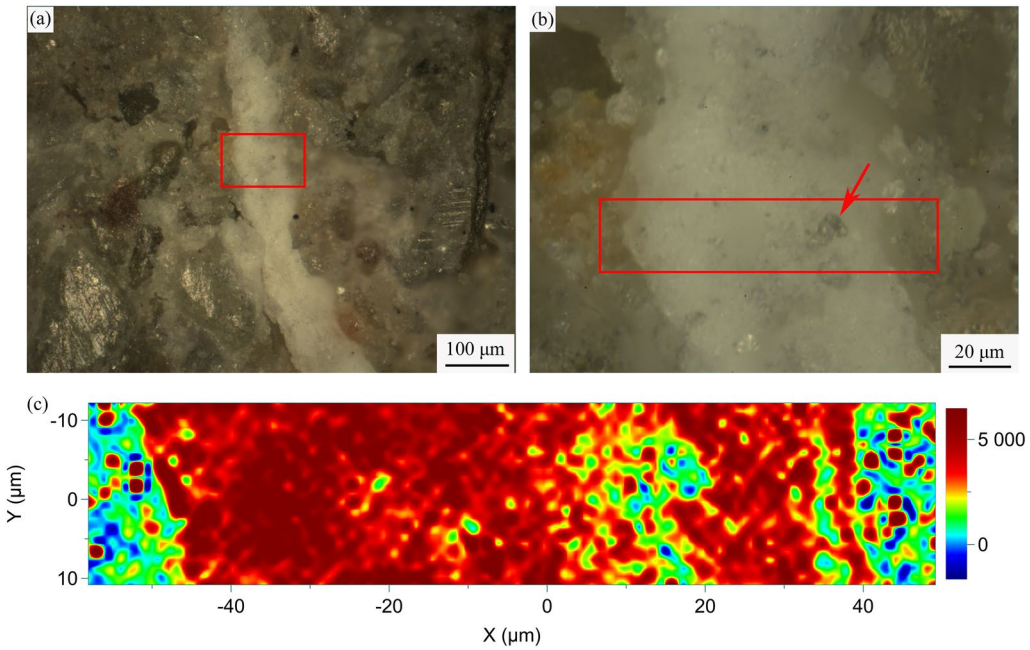

Fig. 8 Mapping of pterosaur eggshell (sample no. 1b). **a** Optical microscope image. **b** The area selected for Raman mapping (optical microscope image with higher magnification) **c** Raman map position of maximum peak intensity in the region of 963 cm^{-1}, the unique and characteristic peak of fluorapatite. Red represents the highest scores recorded, and blue represents the lowest scores

Another possible explanation for this is that the fluorapatite is the result of phosphatization of soft egg membrane tissues through taphonomic processes after the eggs were buried. Apatite replacement of the membrane testacea is common in fossil eggs [27, 35, 65, 66]. For example, *Antarcticoolithus bradyi*, a giant soft-shelled egg from the Late Cretaceous of Antarctica, is composed of calcium phosphate and is thought to be the result of diagenetic alteration [35]. Phosphatization, as an important taphonomic process of fossil preservation, is the only taphonomic mode that can preserve putative subcellular structures [67]. For example, much-nonmineralized tissue, such as fungi, bacteria, the soft tissue of animals, and coprolites, can be preserved by diagenetic mineralization in apatite [68]. During the phosphatization taphonomic processes, for one thing, the organic tissues, such as the egg membrane, are a potential source of phosphate [67]. In other words, the egg membrane, as the template, naturally synthesized hydroxyapatite, and apatite grew onto the organic template [69–71]. In addition, microbes also play a critical role in phosphatization. First, microbes can release organically bound phosphate from the carcass [72]. Second, microbes can concentrate phosphate [73]. Thus, microbial decay can assist in the phosphatization process [74]. Furthermore, phosphatization of soft tissue can occur within weeks of death [75]. Hence, it is also possible that the apatite of *Hamipterus* eggs is the result of the phosphatization of the membrane.

If fluorapatite is the result of diagenesis, it could therefore conceivably be hypothesized that *H. tianshanensis* may lay soft eggs. Soft eggs, such as secondarily phosphatized *protocertops* [36] and *Antarcticoolithus bradyi* [35], both contain calcium phosphate. In fact, diagenetic alteration of the mineral composition of membrane testacea to apatite is relatively common in fossil eggs [27, 65, 66]. Hence, it may be that *H. tianshanensis* lays soft eggs and that fluorapatite is the phosphatization result of membrane testacea.

Overall, the special phenomenon that white pterosaur eggshell is composed of fluorapatite can be explained either by the biomineral source, similar to living *S. merianae* eggshells, or by phosphatization taphonomic processes. Regardless of which explanation is correct, our studies provided more information about pterosaur eggs. After all, fluorapatite pterosaur eggshell has not previously been described. In reviewing the literature, most pterosaur egg studies focus on morphologic analysis [41–49]. To date, only Grellet-Tinner et al. reported the composition of a three-dimensional pterosaur egg (*Pterodaustro guinazui*, from central Argentina) [47]. The eggshell thickness averages 50 μm, which is consistent with the eggs of *H. tianshanensis* in this study [47]. However, the mineral composition of eggshells between

Pterodaustro guinazui and *H. tianshanensis* is different. The mineral composition of *H. tianshanensis* eggshell is apatite, while the eggshell of *P. guinazui* consists of calcium carbonate [47]. Thus, it can be indicated that the high compositional variation among pterosaur eggshells is due to the different mineral eggshell compositions between *P. guinazui* and *H. tianshanensis*.

According to these data, it can be inferred that the mineral composition of pterosaur eggshell is complicated and cannot be simply deduced by extant phylogenetic bracketing. Because the discovery of pterosaur eggs is so rare, the mineral composition of pterosaur eggs is mainly deduced by extant phylogenetic bracketing. Based on phylogenetic analyses, it is generally assumed that pterosaur is the sister taxon to Dinosauria, forming the clade Ornithodira (Avemetatarsalia) [76]. Moreover, the clade including pterosaurs, dinosaurs, and birds is a sister clade to one that contains extant crocodiles [39]. Since crocodile dinosaurs and birds all lay eggs with a calcium carbonate shell, it is most reasonable that pterosaurs also laid eggs with a calcium carbonate shell. However, a recent study by Norell et al. [36] revealed that the first dinosaur egg was soft-shelled. Hence, egg evolution among crocodiles, dinosaurs, and pterosaurs must be complicated. Furthermore, the assumption that the mineral composition of pterosaur eggs is $CaCO_3$ may be modified.

However, this study remains limited due to the small number of samples. Since laboratory analysis requires samples to be removed from large specimens, which is harmful, a portable Raman spectrometer in the field may be a better method for future research.

The finding that the mineral composition for *H. tianshanensis* eggshell is fluorapatite, while preliminary, is significant in at least two major respects. First, this study rectifies the formal view that calcite is the main component of *Hamipterus* eggshell. In fact, the eggshell is mainly composed of fluorapatite and without calcite. Second, the fluorapatite eggshell can be explained either by biomineral or diagenetic alteration. Regardless of which explanation is correct, this finding indicated that the *Hamipterus* reproduction pattern is special.

Conclusions

In this investigation, the aim was to determine the minerals that existed in *Hamipterus* eggshells. The SEM–EDS elemental mapping shows that Ca and P have similar distribution patterns among the eggshells. The Raman spectroscopy results show an obvious intense peak of approximately 966 cm^{-1} among the white eggshell, which can be hard evidence of calcium phosphate in *H. pterosaur* eggs. Moreover, no intense peaks of calcite can be observed in eggshells. Combined with the existence of F in the eggshell, it can be assumed that the main mineral of *H. pterosaur* eggshell is fluorapatite $Ca_5(PO_4)_3F$.

The fluorapatite $Ca_5(PO_4)_3F$ in the eggshell can be explained in two ways. One possibility is that the fluorapatite is biomineral source, and the bioapatite transformed to fluorapatite over geological time. This means that *H. tianshanensis* laid apatite-shelled eggs, similar to living *S. merianae*. Another explanation is that the fluorapatite is the result of phosphatization taphonomic processes, indicating that *H. tianshanensis* may lay soft eggs. More work and specimens are necessary to confirm either explanation.

In any case, these remarkable findings contribute to our understanding of the mineral composition of pterosaur eggshells and offer some insight into the nature of the eggshell and even pterosaur reproduction pattern.

Author contributions

Conceptualization, YL, WL, QW and XZ; methodology, YL and XZ; software, YL; validation, YL, YY, XZ, WL and XW; formal analysis, YL; investigation, YL; resources, WL and XW; data curation, YL, XZ and WL; writing—original draft preparation, YL; writing—review and editing, YL, YY, XZ, QW, SJ, WL and XW; visualization, YL; supervision, YL, YY, XZ, QW, SJ, WL and XW; project administration, W L and XW; funding acquisition, WL and XW. All authors have read and approved the final manuscript.

Funding

This work was funded by the National Social Science Fund of China under Grant number 20VJXG018, the Beijing Municipal Social Science Foundation (No. 21DTR046), the National Natural Science Foundation under Grant numbers 42288201 and 41572020, the Fundamental Research Funds for the Central Universities (E1E40905X2) and the Hami City Government Cooperation Project.

Data availability

Not applicable.

Declarations

Competing interests

The authors declare no competing interests.

Author details

[1]Department of Archaeology and Anthropology, University of Chinese Academy of Sciences, Beijing 100049, China. [2]Key Laboratory of Vertebrate Evolution and Human Origins of Chinese Academy of Sciences, Institute of Vertebrate Paleontology and Paleoanthropology, Chinese Academy of Sciences, Beijing 100044, China. [3]College of Earth and Planetary Sciences, University of Chinese Academy of Sciences, Beijing 100049, China. [4]CAS Center for Excellence in Life and Paleoenvironment, Beijing 100044, China.

Received: 28 January 2022 Accepted: 21 May 2022
Published online: 14 June 2022

References

1. Fan X, Wang Q, Wang Y. Non-destructive in situ Raman spectroscopic investigation of corrosion products on the bronze dagger-axes from Yujiaba site in Chongqing. China Archaeol Anthropol Sci. 2020;12:90. https://doi.org/10.1007/s12520-020-01042-0.
2. Wang X, Zhen G, Hao X, Tong T, Ni F, Wang Z, Jia J, Li L, Tong H. Spectroscopic investigation and comprehensive analysis of the polychrome clay

sculpture of Hua Yan Temple of the Liao Dynasty. Spectrochim Acta Part A Mol Biomol Spectrosc. 2020;240: 118574. https://doi.org/10.1016/j.saa.2020.118574.
3. Li T, Liu C, Wang D. Applying micro-computed tomography (micro-CT) and Raman spectroscopy for non-invasive characterization of coating and coating pigments on ancient Chinese papers. Herit Sci. 2020;8:22. https://doi.org/10.1186/s40494-020-00366-3.
4. Jin P, Yao Z, Zhang M, Li Y, Xing H. A pigment (CuS) identified by micro-Raman spectroscopy on a Chinese funerary lacquer ware of West Han Dynasty. J Raman Spectrosc. 2010;41:222–5. https://doi.org/10.1002/jrs.2412.
5. Cheng X, Xia Y, Ma Y, Lei Y. Three fabricated pigments (Han purple, indigo and emerald green) in ancient Chinese artifacts studied by Raman microscopy, energy-dispersive X-ray spectrometry and polarized light microscopy. J Raman Spectrosc. 2007;38:1274–9. https://doi.org/10.1002/jrs.1766.
6. Giuffrida D, Mollica Nardo V, Neri D, Cucinotta G, Calabrò IV, Pace L, Ponterio RC. A multi-analytical study for the enhancement and accessibility of archaeological heritage: the churches of San Nicola and San Basilio in Motta Sant'Agata (RC, Italy). Remote Sens. 2021;13:3738. https://doi.org/10.3390/rs13183738.
7. Xia Y, Ma Q, Zhang Z, Liu Z, Feng J, Shao A, Wang W, Fu Q. Development of Chinese barium copper silicate pigments during the Qin Empire based on Raman and polarized light microscopy studies. J Archaeol Sci. 2014;49:500–9. https://doi.org/10.1016/j.jas.2014.05.035.
8. Chen P, Wang F, Luo H, Zhu J, Shi P, Wang T. Nondestructive study of glassy matrix of celadons prepared in different firing temperatures. J Raman Spectrosc. 2021;52:1360–70. https://doi.org/10.1002/jrs.6132.
9. Wang R, Li Y. Multiexcitation Raman Spectroscopy in Identification of Chinese Jade. Spectrosc Lett. 2011;44:432–9. https://doi.org/10.1080/00387010.2011.577885.
10. Bruni Y, Hatert F, George P, Strivay D. An archaeometric investigation of glass beads decorating the reliquary of Saint Simètre from Lierneux, Belgium. J Archaeol Sci Rep. 2020;32: 102451. https://doi.org/10.1016/j.jasrep.2020.102451.
11. Rouchon V, Badet H, Belhadj O, Bonnerot O, Lavédrine B, Michard J-G, Miska S. Raman and FTIR spectroscopy applied to the conservation report of paleontological collections: identification of Raman and FTIR signatures of several iron sulfate species such as ferrinatrite and sideronatrite. J Raman Spectrosc. 2012;43:1265–74. https://doi.org/10.1002/jrs.4041.
12. Witke K, Götze J, Rößler R, Dietrich D, Marx G. Raman and cathodoluminescence spectroscopic investigations on Permian fossil wood from Chemnitz—a contribution to the study of the permineralisation process. Spectrochim Acta Part A Mol Biomol Spectrosc. 2004;60:2903–12. https://doi.org/10.1016/j.saa.2003.12.045.
13. Da Silva JH, Saraiva GD, Memória Campelo SC, Cisneros Martínez JC, Viana BC, Bezerra FI, Abagaro BTO, Cavalcante Freire PT. Raman and infrared spectroscopy investigation of the root fossil (rhizoliths) from the Carboniferous period, Piauí Formation, Parnaíba Sedimentary Basin, Northeast Brazil. Vib Spectrosc. 2019;100:117–22. https://doi.org/10.1016/j.vibspec.2018.11.007.
14. Bezerra FI, Da Silva JH, Miguel EDC, Paschoal AR, Nascimento DR, Freire PTC, Viana BC, Mendes M. Chemical and mineral comparison of fossil insect cuticles from Crato Konservat Lagerstätte, Lower Cretaceous of Brazil. J Iber Geol. 2020;46:61–76. https://doi.org/10.1007/s41513-020-00119-y.
15. Schopf JW, Kudryavtsev AB. Confocal laser scanning microscopy and Raman imagery of ancient microscopic fossils. Precambr Res. 2009;173:39–49. https://doi.org/10.1016/j.precamres.2009.02.007.
16. Chen J-Y, Schopf JW, Bottjer DJ, Zhang C-Y, Kudryavtsev AB, Tripathi AB, et al. Raman spectra of a Lower Cambrian ctenophore embryo from southwestern Shaanxi, China. Proc Natl Acad Sci. 2007;104:6289–92. https://doi.org/10.1073/pnas.0701246104.
17. Akse SP, Das G, Agustí S, Pichevin L, Polerecky L, Middelburg JJ. Imaging of organic signals in individual fossil diatom frustules with nanoSIMS and Raman spectroscopy. Mar Chem. 2021;228: 103906. https://doi.org/10.1016/j.marchem.2020.103906.
18. Osés G, Petri S, Voltani CG, Prado G, Galante D, Rizzutto MA, et al. Deciphering pyritization-kerogenization gradient for fish soft-tissue preservation. Sci Rep. 2017;7:1468.
19. Wiemann J, Fabbri M, Yang T-R, Stein K, Sander PM, Norell MA, Briggs DEG. Fossilization transforms vertebrate hard tissue proteins into N-heterocyclic polymers. Nat Commun. 2018;9:4741. https://doi.org/10.1038/s41467-018-07013-3.
20. Thomas DB, Fordyce RE, Frew RD, Gordon KC. A rapid, non-destructive method of detecting diagenetic alteration in fossil bone using Raman spectroscopy. J Raman Spectrosc. 2007;38:1533–7. https://doi.org/10.1002/jrs.1851.
21. Thomas DB, Mcgoverin CM, Fordyce RE, Frew RD, Gordon KC. Raman spectroscopy of fossil bioapatite—a proxy for diagenetic alteration of the oxygen isotope composition. Palaeogeogr Palaeoclimatol Palaeoecol. 2011;310:62–70. https://doi.org/10.1016/j.palaeo.2011.06.016.
22. Yang TR, Wiemann J, Xu L, Cheng YN, Sander M. Reconstruction of oviraptorid clutches illuminates their unique nesting biology. Acta Palaeontol Pol. 2019. https://doi.org/10.4202/app.00497.2018.
23. Kim N-H, Choi S, Kim S, Lee Y-N. A new faveoloolithid oogenus from the Wido Volcanics (Upper Cretaceous), South Korea and a new insight into the oofamily Faveoloolithidae. Cretac Res. 2019;100:145–63. https://doi.org/10.1016/j.cretres.2019.04.001.
24. Moreno-Azanza M, Bauluz B, Canudo JI, Gasca JM, Fernández-Baldor F. Combined use of electron and light microscopy techniques reveals false secondary shell units in Megaloolithidae eggshells. PLoS ONE. 2016;11: e0153026.
25. Elejalde-Cadena NR, Estevez JO, Torres-Costa V, Ynsa-Alcalá MD, García-López G, Moreno A. Molecular analysis of the mineral phase and examination of possible intramineral proteins of dinosaur eggshells collected in El Rosario, Baja California Mexico. ACS Earth Space Chem. 2021;5:1552–63. https://doi.org/10.1021/acsearthspacechem.1c00077.
26. Yang T-R, Chen Y-H, Wiemann J, Spiering B, Sander PM. Fossil eggshell cuticle elucidates dinosaur nesting ecology. PeerJ. 2018;6: e5144. https://doi.org/10.7717/peerj.5144.
27. Stein K, Prondvai E, Huang T, Baele J-M, Sander PM, Reisz R. Structure and evolutionary implications of the earliest (Sinemurian, early Jurassic) dinosaur eggs and eggshells. Sci Rep. 2019;9:4424. https://doi.org/10.1038/s41598-019-40604-8.
28. Shawkey MD, D'alba L. Egg pigmentation probably has an early Archosaurian origin. Nature. 2019;570:E43–5. https://doi.org/10.1038/s41586-019-1282-4.
29. Wiemann J, Yang T-R, Norell MA. Reply to: egg pigmentation probably has an Archosaurian origin. Nature. 2019;570:E46–50. https://doi.org/10.1038/s41586-019-1283-3.
30. Wiemann J, Yang T-R, Norell MA. Dinosaur egg colour had a single evolutionary origin. Nature. 2018;563:555–8. https://doi.org/10.1038/s41586-018-0646-5.
31. Wiemann J, Crawford JM, Briggs DEG. Phylogenetic and physiological signals in metazoan fossil biomolecules. Sci Adv. 2020;6:eaba6883. https://doi.org/10.1126/sciadv.aba6883.
32. Choi S, Lee SK, Kim N-H, Kim S, Lee Y-N. Raman spectroscopy detects amorphous carbon in an enigmatic egg from the upper Cretaceous Wido Volcanics of South Korea. Front Earth Sci. 2020. https://doi.org/10.3389/feart.2019.00349.
33. Choi S, Park Y, Kweon JJ, Kim S, Jung H, Lee SK, Lee Y-N. Fossil eggshells of amniotes as a paleothermometry tool. Palaeogeogr Palaeoclimatol Palaeoecol. 2021;571:110376. https://doi.org/10.1016/j.palaeo.2021.110376.
34. Hirsch KF. Parataxonomic classification of fossil chelonian and gecko eggs. J Vertebr Paleontol. 1996;16:752–62. https://doi.org/10.1080/02724634.1996.10011363.
35. Legendre LJ, Rubilar-Rogers D, Musser GM, Davis SN, Otero RA, Vargas AO, Clarke JA. A giant soft-shelled egg from the late Cretaceous of Antarctica. Nature. 2020;583:411–4. https://doi.org/10.1038/s41586-020-2377-7.
36. Norell MA, Wiemann J, Fabbri M, Yu C, Marsicano CA, Moore-Nall A, Varricchio DJ, Pol D, Zelenitsky DK. The first dinosaur egg was soft. Nature. 2020;583:406–10. https://doi.org/10.1038/s41586-020-2412-8.
37. Choi S, Han S, Kim N-H, Lee Y-N. A comparative study of eggshells of Gekkota with morphological, chemical compositional and crystallographic approaches and its evolutionary implications. PLoS ONE. 2018;13: e0199496. https://doi.org/10.1371/journal.pone.0199496.
38. Wang X, Kellner AA, Jiang S, Wang Q, Ma Y, Paidoula Y, et al. Sexually dimorphic tridimensionally preserved pterosaurs and their eggs. Curr Biol. 2014;24:1323–30.

39. Martill DM. Palaeontology: which came first, the pterosaur or the egg? Curr Biol. 2014;24:R615–7. https://doi.org/10.1016/j.cub.2014.05.040.
40. Wang X, Kellner A, Jiang S, Cheng X, Wang Q, Ma Y, et al. Egg accumulation with 3D embryos provides insight into the life history of a pterosaur. Science. 2017;358:1197.
41. Chiappe LM, Codorniú L, Grellet-Tinner G, Rivarola D. Argentinian unhatched pterosaur fossil. Nature. 2004;432:571–2. https://doi.org/10.1038/432571a.
42. Ji Q, Ji S-A, Cheng Y-N, You H-L, Lü J-C, Liu Y-Q, Yuan C-X. Pterosaur egg with a leathery shell. Nature. 2004;432:572–572. https://doi.org/10.1038/432572a.
43. Wang X, Zhou Z. Pterosaur embryo from the Early Cretaceous. Nature. 2004;429:621.
44. Grellet-Tinner G, Wroe S, Thompson MB, Ji Q. A note on pterosaur nesting behavior. Hist Biol. 2007;19:273–7. https://doi.org/10.1080/08912960701189800.
45. Unwin D, Charles D. Pterosaur eggshell structure and its implications for pterosaur reproductive biology. Zitteliana. 2008;2008:199–207.
46. Lü J, Unwin DM, Deeming DC, Jin X, Liu Y, Ji Q. An egg-adult association, gender, and reproduction in pterosaurs. Science. 2011;331:321–4.
47. Grellet-Tinner G, Thompson MB, Fiorelli LE, Argañaraz E, Codorniú L, Hechenleitner EM. The first pterosaur 3-D egg: Implications for *Pterodaustro guinazui* nesting strategies, an Albian filter feeder pterosaur from central Argentina. Geosci Front. 2014;5:759–65. https://doi.org/10.1016/j.gsf.2014.05.002.
48. Wang X, Kellner AWA, Cheng X, Jiang S, Wang Q, Sayao JM, et al. Eggshell and histology provide insight on the life history of a pterosaur with two functional ovaries. Annals Brazilian Acad Sci. 2015;87:1599–609.
49. Codorniú L, Chiappe L, Rivarola D. Neonate morphology and development in pterosaurs: evidence from a Ctenochasmatid embryo from the Early Cretaceous of Argentina. Geol Soc Lond Special Publ. 2017;455:83–94.
50. Eberth D, Brinkman D, Chen P, Yuan F, Wu S, Li G, Cheng X. Sequence stratigraphy, paleoclimate patterns, and vertebrate fossil preservation in Jurassic-Cretaceous strata of the Junggar Basin, Xinjiang autonomous region, People. Canadian J Earth Sci. 2001;38:1627–44.
51. Li Y, Luo W, Yang Y, Jiang S, Wang X. A preliminary study of the weathering mechanism of fossilized Cretaceous *Hamipterus* bones. Sci China Earth Sci. 2021. https://doi.org/10.1007/s11430-020-9702-8.
52. Han X, Zhao W, Chen C, Jiang S, Wang X. Study on the unusual weathering of the bones and eggs accumulation with embryos fossils of *Hamipterus tianshanensis*. Geol Rev. 2022;68:81–92.
53. Khan AF, Awais M, Khan AS, Tabassum S, Chaudhry AA, Rehman IU. Raman spectroscopy of natural bone and synthetic apatites. Appl Spectrosc Rev. 2013;48:329–55. https://doi.org/10.1080/05704928.2012.721107.
54. Yu H, Zhang H, Wang X, Gu Z, Li X, Deng F. Local structure of hydroxy–peroxy apatite: a combined XRD, FT-IR, Raman, SEM, and solid-state NMR study. J Phys Chem Solids. 2007;68:1863–71. https://doi.org/10.1016/j.jpcs.2007.05.020.
55. O'shea DC, Bartlett ML, Young RA. Compositional analysis of apatites with laser-Raman spectroscopy: (OH, F, Cl) apatites. Arch Oral Biol. 1974;19:995–1006. https://doi.org/10.1016/0003-9969(74)90086-7.
56. Liu Y, Wang A, Freemen JJ. 2009. Raman, MIR, and NIR Spectroscopic Study of Calcium Sulfates: Gypsum, Bassanite, and Anhydrite. In Proceedings of the Lunar and Planetary Science Conference, March 01 2009.
57. Jehlička J, Vítek P, Edwards HGM, Hargreaves MD, Čapoun T. Fast detection of sulphate minerals (gypsum, anglesite, baryte) by a portable Raman spectrometer. J Raman Spectrosc. 2009;40:1082–6. https://doi.org/10.1002/jrs.2246.
58. Foucher F, Ammar M-R, Westall F. Revealing the biotic origin of silicified Precambrian carbonaceous microstructures using Raman spectroscopic mapping, a potential method for the detection of microfossils on Mars. J Raman Spectrosc. 2015;46:873–9. https://doi.org/10.1002/jrs.4687.
59. Hincke M, Nys Y, Gautron J, Mann K, Rodriguez-Navarro A, Mckee M. The eggshell: structure, composition and mineralization. Front Biosci. 2012;17:1266–80.
60. Mikhailov K. Classification of fossil eggshells of amniotic vertebrates. Acta Palaeontol Pol. 1991;36:193–238.
61. Campos-Casal FH, Cortez Francisco A, Gomez EI, Chamut SN. Chemical composition and microstructure of recently oviposited eggshells of *Salvator merianae* (Squamata: Teiidae). Herpetol Conserv Biol. 2020;15:25–40.
62. Campos-Casal FH, Gomez EI, Cortez FA, Chamut SN. Hialuronic acid in the eggshell of *Salvator merianae* (Squamata: Teiidae). Rev Agron Noroeste Argent. 2020;40:111–22.
63. Yi H, Balan E, Gervais C, Ségalen L, Roche D, Person A, Fayon F, Morin G, Babonneau F. Probing atomic scale transformation of fossil dental enamel using Fourier transform infrared and nuclear magnetic resonance spectroscopy: a case study from the Tugen Hills (Rift Gregory, Kenya). Acta Biomater. 2014;10:3952–8. https://doi.org/10.1016/j.actbio.2013.12.049.
64. Kim T, Lee Y, Lee Y-N. Fluorapatite diagenetic differences between Cretaceous skeletal fossils of Mongolia and Korea. Palaeogeogr Palaeoclimatol Palaeoecol. 2018;490:579–89. https://doi.org/10.1016/j.palaeo.2017.11.047.
65. Grellet-Tinner G, Codrea V, Folie A, Higa A, Smith T. First evidence of reproductive adaptation to "island effect" of a dwarf Cretaceous Romanian titanosaur, with embryonic integument in ovo. PLoS ONE. 2012;7: e32051. https://doi.org/10.1371/journal.pone.0032051.
66. Prondvai E, Botfalvai G, Stein K, Szentesi Z, Ősi A. Collection of the thinnest: a unique eggshell assemblage from the Late Cretaceous vertebrate locality of Iharkút (Hungary). Cent Eur Geol. 2017;60:73–133. https://doi.org/10.1556/24.60.2017.004.
67. Schiffbauer JD, Wallace AF, Broce J, Xiao S. Exceptional fossil conservation through phosphatization. Paleontol Soc Pap. 2014;20:59–82. https://doi.org/10.1017/S1089332600002801.
68. Lucas J, Prevot LE. Phosphates and fossil preservation. In: Allison PA, Briggs DEG, editors. Taphonomy: releasing the data locked in the fossil record. New York: Plenum press; 1991.
69. Ramdan RD, Sunendar B, Hermawan H. Naturally derived biomaterials and its processing. In: Mahyudin F, Hermawan H, editors. Biomaterials and medical devices: a perspective from an emerging country. Cham: Springer International Publishing; 2016. p. 23–39.
70. Sabu U, Logesh G, Rashad M, Joy A, Balasubramanian M. Microwave assisted synthesis of biomorphic hydroxyapatite. Ceram Int. 2019;45:6718–22. https://doi.org/10.1016/j.ceramint.2018.12.161.
71. Zhang Y, Liu Y, Ji X, Banks CE, Song J. Flower-like agglomerates of hydroxyapatite crystals formed on an egg-shell membrane. Colloids Surf. 2011;82:490–6. https://doi.org/10.1016/j.colsurfb.2010.10.006.
72. Wilby PR, Briggs DEG. Taxonomic trends in the resolution of detail preserved in fossil phosphatized soft tissues. Geobios. 1997;30:493–502. https://doi.org/10.1016/S0016-6995(97)80056-3.
73. Briggs DEG, Wilby PR. The role of the calcium carbonate-calcium phosphate switch in the mineralization of soft-bodied fossils. J Geol Soc. 1996;153:665–8. https://doi.org/10.1144/gsjgs.153.5.0665.
74. Wilby PR, Briggs DEG, Bernier P, Gaillard C. Role of microbial mats in the fossilization of soft tissues. Geology. 1996;24:787–90. https://doi.org/10.1130/0091-7613(1996)024%3c0787:Rommit%3e2.3.Co;2.
75. Briggs DEG, Kear AJ, Martill DM, Wilby PR. Phosphatization of soft-tissue in experiments and fossils. J Geol Soc London. 1993;150:1035–8. https://doi.org/10.1144/gsjgs.150.6.1035.
76. Benton MJ. *Scleromochlus taylori* and the origin of dinosaur and pterosaurs. Philos Trans Royal Soc Biol Sci. 1999;354:1423–46.

Publisher's Note